



In situ fabrication $\text{Ti}_3\text{C}_2\text{F}_x$ MXene/ CdIn_2S_4 Schottky junction for photocatalytic oxidation of HMF to DFF under visible light

Ming Zhang^a, Yuxin Zhang^a, Lei Ye^a, Zhihao Yu^a, Runyu Liu^a, Yina Qiao^c, Linhao Sun^a, Jifang Cui^a, Xuebin Lu^{b,*}

^a School of Environmental Science and Engineering, Tianjin University, Tianjin 30000, PR China

^b School of Science, Tibet University, Lhasa 850000, PR China

^c School of Environment and Safety Engineering, North University of China, Taiyuan, PR China

ARTICLE INFO

Keywords:

CdIn_2S_4

MXene

Schottky junction

Value-added conversion

ABSTRACT

It is highly demanded to steer the charge flow in semiconductors for efficient photocatalytic selective value-added conversion. In this study, we designed an interfacial contact Ti_3C_2 MXene/ CdIn_2S_4 Schottky heterostructure which could greatly enhance the photogenerated charge separation of CdIn_2S_4 . The study found that MXene/ CdIn_2S_4 Schottky junction and ultra-thin nanostructures greatly promote the efficiency of photogenerated carriers separation and interface transfer. Compared with pure CIS, this heterostructure showed more excellent and stable HMF value-added conversion performance under natural conditions (DFF yield increased by 2.3 times). This work provides a new idea for MNs-based Schottky junction construction and a promising method for the photocatalytic value-added conversion of biomass under natural conditions.

1. Introduction

Reducing our dependence on fossil resources, except for renewable energy production, is as important as exploring renewable carbon sources [1]. In this regard, biomass has been listed as one of the sustainable carbon sources' unique candidates [2,3]. The catalytic conversion of biomass-based platform compounds was an important use of biomass resources [4–6]. 5-hydroxymethylfurfural (HMF) has especially high application potential among many platform compounds. Through catalytic oxidation, HMF can be further transformed into important furan products, including 2,5-diformylfuran (DFF) and 2,5-furan dicarboxylic acid (FDCA) [7]. Particularly, several methods for DFF to synthesize a series of high-value chemicals with broad market prospects have been studied [8,9]. Thus, it is essential to develop environmentally friendly and excellent efficiency catalytic approaches for oxidation HMF to DMF under the conditions of mildness, which is regarded as a pressing of production practices. Among various strategies for sustainable value-added transformation from HMF to DFF, the cheapest and easiest characteristics have been assigned to photocatalysis [10–14].

Researchers have gained attention under photocatalysts techniques such as TiO_2 [15–17], CdS [18], CdIn_2S_4 [19] and g- C_3N_4 [20] to prove their practicable and efficiency. Among them, CdIn_2S_4 (CIS) is a

potential photocatalytic material [21]. However, the catalytic conversion efficiency of pure CIS material from HMF to DFF under natural conditions is not ideal [19]. The process of Photocatalytic selective oxidation of HMF could be divided into three steps: light absorption, charge transfer, and interfacial reaction, while the causes for the inferior conversion efficiency are as follows: 1) Less efficient use of sunlight, 2) Photogenerated electron-hole ($e^- - h^+$) pairs recombination rate is high, photogenerated carrier separation and migration efficiency are low, 3) Insufficient surface active sites [22]. Among them, efficacious means to resolve these three problems were to adopt cocatalysts modified by the semiconductor photocatalysts [23,24].

MXenes (MNs) as a new type of two-dimensional nanomaterials have been widely emphasized to further improve photocatalytic activity because their outstanding electron mobility will facilitate the separation of $e^- - h^+$ and abundant functional groups will be convenient to couple with other materials [25–28]. Here, ultra-thin MNs nanosheets were obtained by selectively etching Al atoms under the layered precursor Ti_3AlC_2 . MNs/CIS heterostructure was obtained by in situ growth of CIS on MNs surface. Under natural conditions, HMF conversion to DFF by photocatalytic oxidation, the yield of DFF was about 2.3 times higher than that of original CIS when the MNs incorporated, besides the activity remained unchanged after 5 cycles. The experiments revealed that the

* Corresponding author.

E-mail address: xbltju@tju.edu.cn (X. Lu).

<https://doi.org/10.1016/j.apcatb.2023.122635>

Received 8 January 2023; Received in revised form 2 March 2023; Accepted 13 March 2023

Available online 15 March 2023

0926-3373/© 2023 Elsevier B.V. All rights reserved.

improvement of photocatalytic performance was ascribed to the lower photogenerated $e^- - h^+$ pair recombination efficiency, higher photogenerated carrier separation, migration efficiency, and more active sites provided by MNs. This work proves that MNs are an effective cocatalyst for biomass platform molecules in photocatalytic value-added transformation and offers a novel idea for constructing a CIS-based Schottky junction.

2. Experimental work

2.1. MNs nanosheets preparation

MAX phase powder (2 g) was slowly added into HCl aqueous solution (20 mL, 9 M) containing LiF (2 g) for 30 min to prevent excessive heating owing to the process will release heat. Then, the reaction was carried out under the condition of consecutive stirring for 48 h. Add 10 mL 2 M H_2SO_4 and mix well after stirring. The obtained products were collected by centrifuge and then washed several times with deionized water until the pH value approached 6. The resultant product was ultrasonicated in an ice bath for 30 min to afford delaminated MNs. At last, samples were collected by centrifugation and dried at 60 °C in a vacuum overnight. And ultra-thin MNs nanosheets with few layers were gotten.

2.2. MNs/CIS heterostructures preparation

A certain amount of ultrathin MNs nanosheets (0, 10, 25, 50, 100, or 200 mg) was ultrasonically dispersed in a 35 mL methanol solution. Then 20 mL of methanol solution of $In(NO_3)_3 \cdot 4 H_2O$ (2 mmol) and $Cd(NO_3)_2 \cdot 4 H_2O$ (1 mmol) was added to the dispersion of MNs nanosheets, the compound was stirred mildly at room temperature for 12 h to guarantee that the positively charged In^{3+} and Cd^{2+} were entirely packaged on the negatively charged MNs nanoflakes. After that, excess thiourea (10 mmol) was added into the mixture and continually stirred for 3 h, and then transferred to a 100 mL autoclave with a Teflon liner (Anhui Kemi Machinery Technology Co., Ltd.), sealed and maintained at 120 °C for 24 h. After natural cooling, centrifugal washing several times. At last, the collected samples were vacuum-dried at 60 °C overnight. For clarity purposes, the samples were labeled as CIS, MNs-1/CIS, MNs-2/CIS, MNs-3/CIS, MNs-4/CIS, MNs-5/CIS.

2.3. Characterization

XRD patterns of the products were obtained from a Bruker AXS D8 diffractometer using $Cu K\alpha$ as the radiation source. The microstructures of as-prepared photocatalysts were characterized by Scanning electron microscopy (SEM, Hitachi SU8010) and Transmission electron microscopy (TEM, JEOL JEM-2100 F). The specific surface area was assessed using a fully automatic specific surface area and a micropore analyzer (ASAP2020, Micromeritics, USA). X-ray Photoelectron Spectroscopy (XPS) spectra were analyzed using a Thermo Fisher Scientific ESCALAB 250 XI. Photoluminescence (PL) spectra were carried out by using an Edinburgh FLS1000/FS5 at room temperature with an excitation wavelength of 330 nm. Time-resolved transient PL decay curves were measured at about 450 nm using the same excitation wavelength by Edinburgh FLS1000/FS5. All electrochemical experiments were conducted on CHI-660E Electrochemical Workstation (Shanghai Chenhua Instrument Co., LTD.). The EPR tests were carried out at room temperature using a JES-FA200 (JEOL) ESR spectrometer performed at X-band frequency.

2.4. Photocatalytic activity tests

Photocatalytic activity of the samples was estimated by the conversion rate of HMF to DFF under a xenon lamp (CEL-HXF3003-T3) coupled to a UV cut filter ($\lambda > 400$ nm) irradiation. Typically, 5 mL of aqueous HMF (10 mM) and 20 mg of catalyst were added into the photoreactors,

at room temperature and with oxygen in the air as the oxidizer.

Afterward, the reactor was stirred intensely (600 rpm) in the dark for 30 min to guarantee the probability of adsorption or reactivity. Connected the water condenser to ensure the reaction system was maintained at 20 °C. The reaction was sustained for 12 h under illumination and agitation. The samples were taken out after 30 min and 12 h were tested in a hermetically sealed vial. The concentration of reactants and resultants were analyzed by a high-performance liquid-chromatography system (Waters, USA) performed with an Aminex HPX-87 H column, using 0.5 mmol/L sulfuric acid as the mobile phase at a flow rate of 0.6 mL/min and equipped with a dual-absorbance detector. Fig. 1.

3. Results and discussion

3.1. Morphology, structure, and optical property

The morphology and structure of the as-prepared photocatalyst can be obtained via SEM (scanning electron microscopy) and TEM (transmission electron microscopy). In Fig. 2a, the stripped MNs present a two-dimensional sheet. Fig. 2b-c presents the SEM images of the CIS sample. It can be found that the CIS sample self-organizes into a spherical morphology. The SEM images of the MNs-3/CIS sample were presented in Fig. 2d-f. Unlike CIS, MNs-3/CIS is a self-organizing flower-like sphere with a puffy appearance. The enlarged view of the spherical surface shows that it is formed from a great number of nanosheets. The thickness of the nanosheets is approximately a few nanometers. There was no characteristic appearance of MNs in the SEM image, so we speculated that in the process of in situ growth of CIS, MNs were further dispersed into smaller nanosheets and combined with CIS to generate nanospheres. To further investigate the element composition and distribution of MNs/CIS, the relevant element mapping was studied, and the distribution of Cd, In, S, Ti, and C elements were represented under different colors, which confirmed the contour of SEM image with uniform distribution of all elements, as shown in Fig. 2h. EDX elemental mapping analysis proved that CIS and MNs were successfully loaded together on the MNs/CIS surface.

In addition, TEM was employed to further highlight the results from the SEM analysis. Pristine MNs (shown in Fig. 3a) present sheet-like morphology accompanies by ultrathin thickness. Fig. S1b and Fig. 3c show the TEM images of CIS and MNs-3/CIS. It can be shown that the surface of CIS was smooth, while the surface of MNs-3/CIS is covered with a large number of nano-sheets. Such structure increases the specific surface area of the material. This is conducive to the contact between materials and reactants in photocatalytic reactions. We also compared the TEM images of heterostructures with different MNs contents (CIS, MNs-1/CIS, MNs-3/CIS, MNs-5/CIS) (Fig. S1). Along with the number of MNs under the heterogeneous gradually increasing (MNs-5/CIS), fewer CIS was surveyed to be grown on the MNs surface, which was difficult to form uniform flower balls (Fig. S1g-h). Upon decreasing the number of MNs adding (MNs-1/CIS), the distribution of CIS is uneven, and some CIS grow alone, which fails to form an effective heterostructure (Fig. S1c-d). Fig. 3d exhibits the high-resolution TEM (HRTEM) image of MNs-3/CIS photocatalyst, indicating that the as-synthesized photocatalyst is a polycrystalline structure. The coexistence of two lattices was observed i.e., CIS (311), CIS (220), and MNs (0110), which indicated tight contact between two materials and the successful generation of the heterostructure. Under the HAADF-STEM elemental mapping, the uniform distribution of Cd, In, S, Ti, and C with the selected area were observed, which further confirmed that the MNs-3/CIS heterostructure was successfully synthesized (Fig. 3 e). The above results of the electron microscopy strongly indicated that between MNs and CIS nanosheets exist uniform and intimate coupling, namely, the successful formation of a heterostructure of ultrathin MNs/CIS nanosheets. Such heterostructure between cocatalyst and photocatalyst endows a large contact area, which improves the interfacial charge transfer efficiency during the

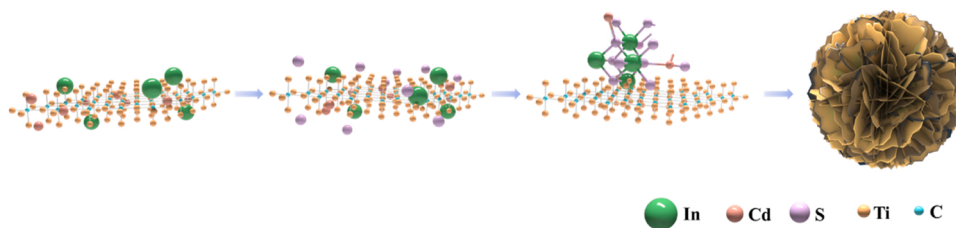


Fig. 1. Illustration for the synthetic process of MNs-CIS.

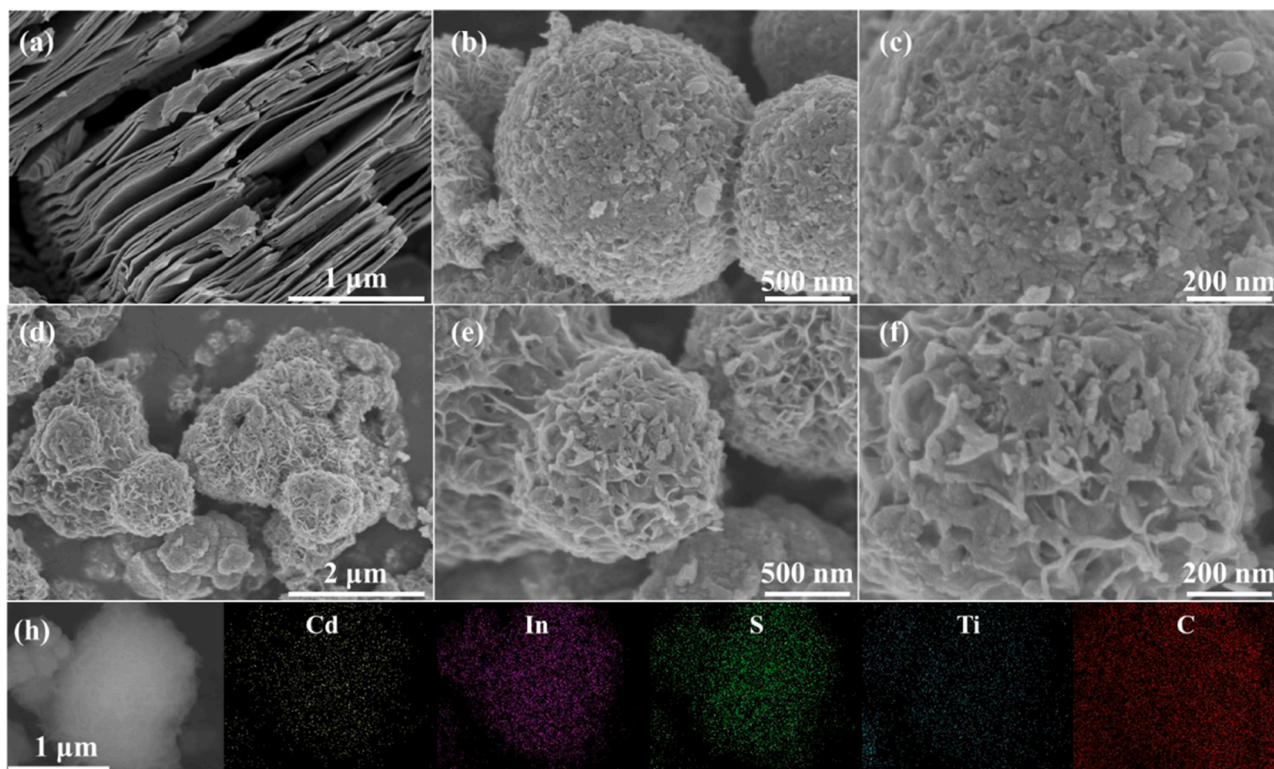


Fig. 2. SEM image of MNs (a), CIS (b-c), MNs-3/CIS (d-f), and the corresponding EDS elemental mappings of Cadmium, Indium, Sulfur, Titanium, and Carbon of MNs-3/CIS (h).

photocatalytic reactions.

X-ray diffraction analysis (XRD) was carried out to research the crystallographic structures of MNs, CIS, MNs-1/CIS, MNs-2/CIS, MNs-3/CIS, MNs-4/CIS, and MNs-5/CIS synthesized under similar conditions, besides, which results are summarized in Fig. 4a. The diffraction peaks are observed at 27.3° , 33.0° , 43.3° , and 47.4° which can be assigned to the (311), (400), (511), and (440) planes of the typical cubic CdIn_2S_4 crystal structure (JCPDS NO.27-0060). Sure enough, the typical diffraction peaks of CIS and MNs were tested in the MNs/CIS heterostructures, and with the increase of MNs proportion, the peak intensity at 18.8, 26.5, 38.5, and 41.6° gradually increased. The XRD data indicate that the MNs/CIS heterostructure exhibited a highly crystalline structure. As shown in Fig. 4b, the X-ray photoelectron spectroscopy (XPS) survey spectrum of MNs-3/CIS displayed the obvious signals including Cd, In, S, C, and Ti. As shown in Fig. S2, there is only a weak signal peak of Ti 2p, which has been detected due to the low dosage of MNs [29] and the superposition of In 3d and Ti 2p [30] under the XPS spectrum. To further support results from the XPS (Fig. 4c), based on inductively coupled plasma-optical emission spectrometry (ICP-OES) and TEM energy-dispersive X-ray spectra (TEM-EDX) we investigated the actual contents of Ti and In in MNs-3/CIS. The results indicated that the Ti and In contents were 2.32% and 53.81%, respectively, which demonstrates

the MNs and CIS were successful integration. (XPS).

The light absorption performance of all synthetic catalysts can be shown by UV visible diffuse reflectance spectroscopy (DRS), from which it can be seen that the absorption edge of CIS has changed after the introduction of MNs (Fig. 4d). For the MNs/CIS heterostructure, the introduction of MNs nanosheets makes the absorption edge of the sample significantly red-shifted. Therefore, the doping effect occurred during the synthetic process of the hybrids. Compared with CIS and MNs-3/CIS, the absorption of the MNs-3/CIS sample was redshifted by about 20 nm Fig. S3, which ascribed to the full-spectrum absorption of MNs. This phenomenon indicates that the MNs/CIS heterostructure absorbs more light from the solar spectrum because of the MNs incorporation. The excellent light absorption ability of MNs/CIS may promote its photocatalytic activity.

3.2. Performance of photocatalytic selective oxidation of HMF

To verify the photocatalytic properties of CIS and MNs/CIS heterostructures and the potential applications of CIS-based heterostructure structures in biomass conversion, we carried out the visible-light-driven catalytic conversion of HMF under mild reaction conditions with atmospheric oxygen as the oxidant. After 12 h, the conversion rate of HMF

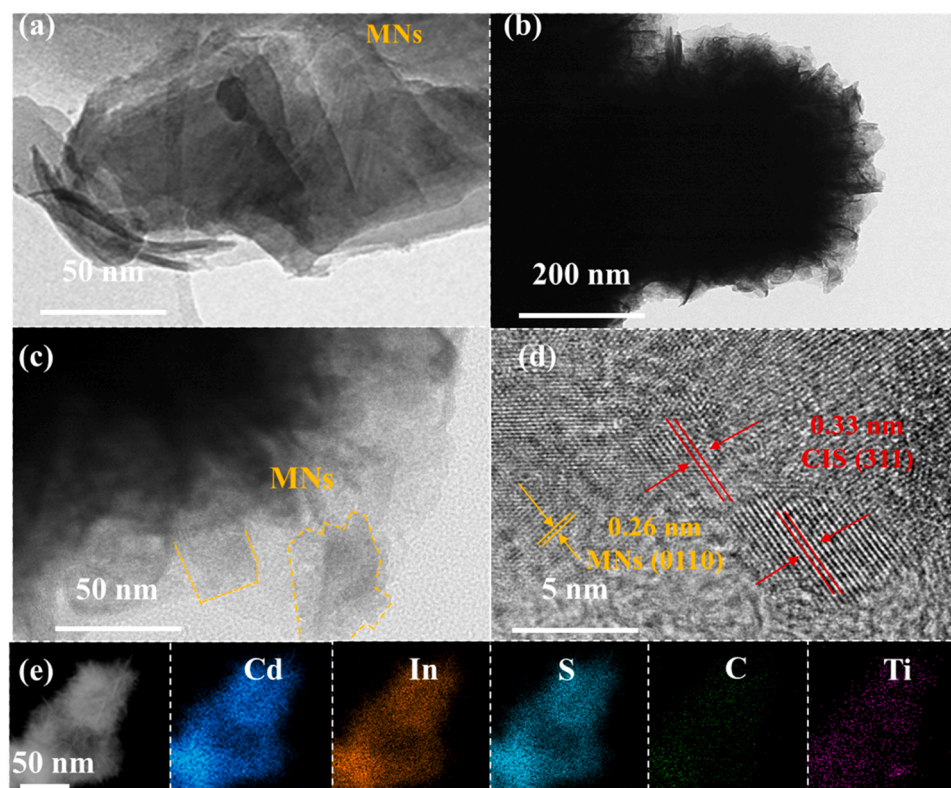


Fig. 3. TEM image of MNs (a) and MNs-3/CIS (b, c), HRTEM image of MNs-3/CIS (d), corresponding element (Cd, In, S, Ti, and C) mapping of MNs-3/CIS (e).

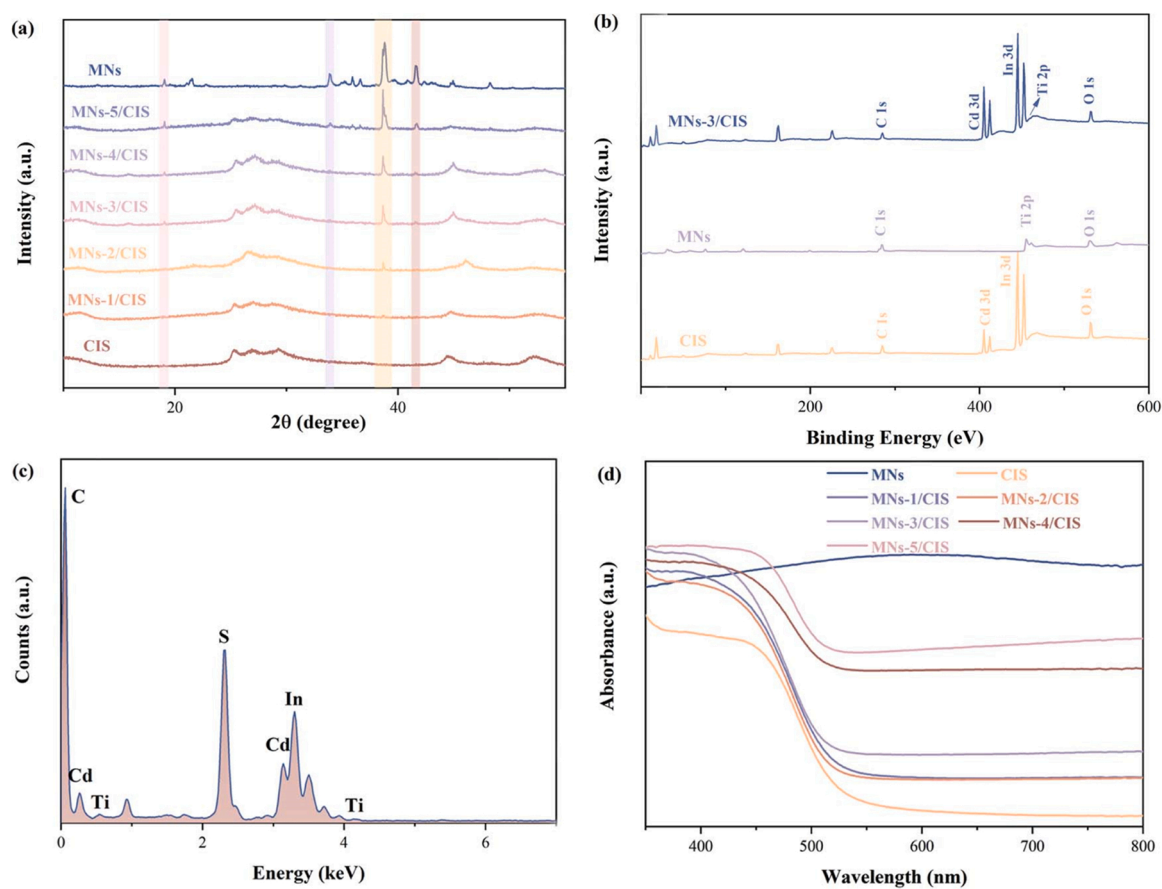


Fig. 4. XRD pattern (a), XPS survey spectra of MNs-3/CIS, MNs, and CIS (b), TEM-EDX spectrum of MNs-3/CIS (c), and UV-vis-NIR DRS spectra (d).

in the original CIS material under visible light irradiation was 35.7%, the selectivity for DFF achieve 72.3%, and the DFF yield reached 25.9%. The low photocatalytic activity was attributed to the sharp recombination of photogenerated $e^- - h^+$ pairs; after the addition of MNs nano-sheets, we successfully enhanced the photocatalytic activity of the heterostructure. The conversion rates of MNs-1/CIS, MNs-2/CIS, MNs-3/CIS, MNs-4/CIS, and MNs-5/CIS, for the photocatalytic oxidation of HMF, were 47.8%, 55.5%, 78.5%, 65.7%, and 58.6%, respectively, and the yields of DFF were 38.6%, 44.6%, 60.3%, 52.3% and 42.3%, respectively (Fig. 5a). The MNs-3/CIS heterostructure demonstrated the best property, which attributes to the optimal ratio between CIS and MNs, the interface effects of the MNs-3/CIS heterostructure, and efficient charge transfer. It is found that the photocatalytic activity was poor when the MNs content is large. We speculate that the reason why the effect of CIS will be inhibited may be that the surface of CIS is intensively covered by excessive MNs. Excessive addition of black MNs results in decreased photoactivity due to the light shielding effect [31]. This inference has been confirmed by the TEM image of MNs-5/CIS (Fig. S1g-h). Table S1 shows that the catalytic conversion efficiency of the MNs-3/CIS heterostructure for HMF, with atmospheric oxygen as the oxidant, is much higher than those of other photocatalytic systems. The stability of the catalyst was a very important parameter under the photocatalysis process; thus, the best and initial materials (MNs-3/CIS and CIS) were investigated via reusing consecutive five-run experiments, the results indicated the conversion rate of HMF over MNs-3/CIS

was nearly unchanged. Compared to the pristine CIS, the HMF conversion rate sharply decrease to 12% after five reaction cycles (Fig. S6a). The stability of the MNs-3/CIS was studied by SEM, XPS, and XRD. As shown in Fig. S6b-c, after the addition of MNs, the morphology, S vacancies, and phase structure were almost unchanged. We performed ICP tests on the solutions before and after the reaction and found that the presence of Cd, In, and S elements was not detected in it (Table S2). During the photocatalytic oxidation process, the efficient separation and migration of charge carriers along the heterogeneous heterostructures and the rapid depletion of carriers reduce the photo corrosion of sulfides, resulting in the excellent stability of MGS-3 /CIS Schottky junctions [32,33].

3.3. Photogenerated carrier transfer mechanism

The matching band structure is the key factor to ensure the photocatalytic reaction. The diagrams of $(\hbar\nu)^{1/2}$ vs. photon energy for CIS are summarized in Fig. 6a. The band gap of CIS is 1.86 eV. The Fermi levels of CIS and MNs were further determined by the Mott-Schottky curve and UV photoelectron spectra (UPS). As shown in Fig. 6b, the Mott-Schottky curve of CIS has a positive slope, so it can be proved that CIS is an n-type semiconductor. According to the intercept of the tangent line of the M-S curve on the X-axis, it can be concluded that the CIS flat band potential is about -0.86 V (vs. Ag/AgCl). CIS as an N-type semiconductor, its conduction band edge is considered to be close to its parity potential, so the CB of CIS is estimated to be 0.66 V (vs. NHE), and the valence band potential is calculated to be 1.20 V (vs. NHE) using the formula of $E_{VB} = E_g - E_{CB}$ [34]. UPS is used to further determine the Fermi level of CIS and the Fermi level and work function of MXene. As shown in Fig. S7, the E_f of MNs was determined to be -0.04 V (vs. NHE), which is more positive than the CB of CIS, indicating that MNs can effectively accept the photogenerated electrons generated by CIS. The UPS shows that the work function of CIS is 4.06 eV and that of MNs is 4.46 eV (vs. absolute vacuum scale, AVS). Theoretically, the electrons of CIS should spontaneously transfer to MNs at the interface of heterojunction, and the E_f of MNs would rise to it aligning with the E_f of CIS. The binding energy of Cd3d, In3d, and S2p under high-resolution XPS spectra of MNs/CIS occurred positive shifts, which illustrate under the heterostructure, the electrons are transferred to MNs from CIS (Fig. S2b-d) [30]. According to the above experimental results, the work function of CIS is lower than MNs, the electrons of CIS would transfer to MNs, to equilibrate the fermi level between the two materials. The Schottky barrier may result from the upward bending of the band of CIS (n-type semiconductor) during the equilibrium process [30,35]. The Schottky junction between them prevents the electrons from returning to CIS on MNs so that the electrons on the MNs are enriched and inhibit the recombination of photogenerated $e^- - h^+$ pairs on CIS, improving the light adsorption and enhancing the charge separation [35].

The separation and migration efficiency of photogenerated carriers and recombination rate of photogenerated $e^- - h^+$ pairs of as-prepared photocatalyst are analyzed by using Photoluminescence (PL) spectroscopy to investigate the effect of MNs incorporation. In general, the efficient recombination of photoexcited charge carriers achieves stronger results with PL intensity [36,37]. In Fig. 6c, compared with the original CIS, the strength of MNs-3/CIS composite decreases to a lower level though the steady-state PL spectrum we observed, which phenomenon indicated that the introduction of MNs significantly improves the efficiency of the composite in separating the photogenerated $e^- - h^+$ pairs [38]. In MNs-3/CIS composites, the excited electrons in CIS are rapidly transferred to MNs due to the conductive properties of MNs. As a result, photogenerated $e^- - h^+$ pairs rapidly separate and inhibit charge recombination, resulting in the quenching of PL intensity. Compared with CIS, MNs-3/CIS showed a significant blue shift between 525 nm and 400 nm, possibly due to the Burstein-moss effect [39,40]. The PL spectrum of MNs-3/CIS displays the main exciton peak and a sharp redshifted emission peak, this may be the incorporation of MNs to

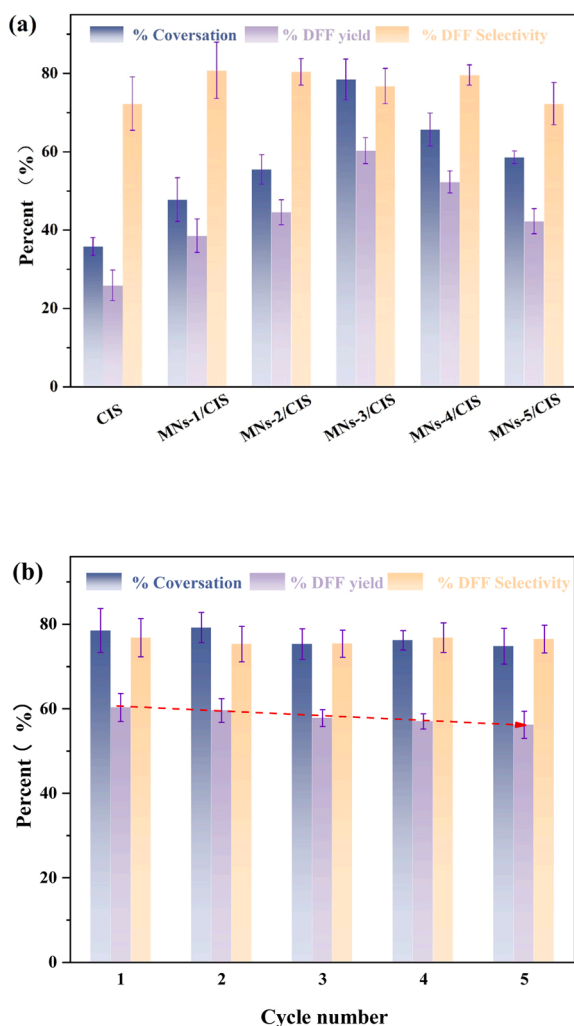


Fig. 5. Performance of the photocatalysts from HMF selective oxidation to DFF (a) and recycle property over MNs-3/CIS (b).

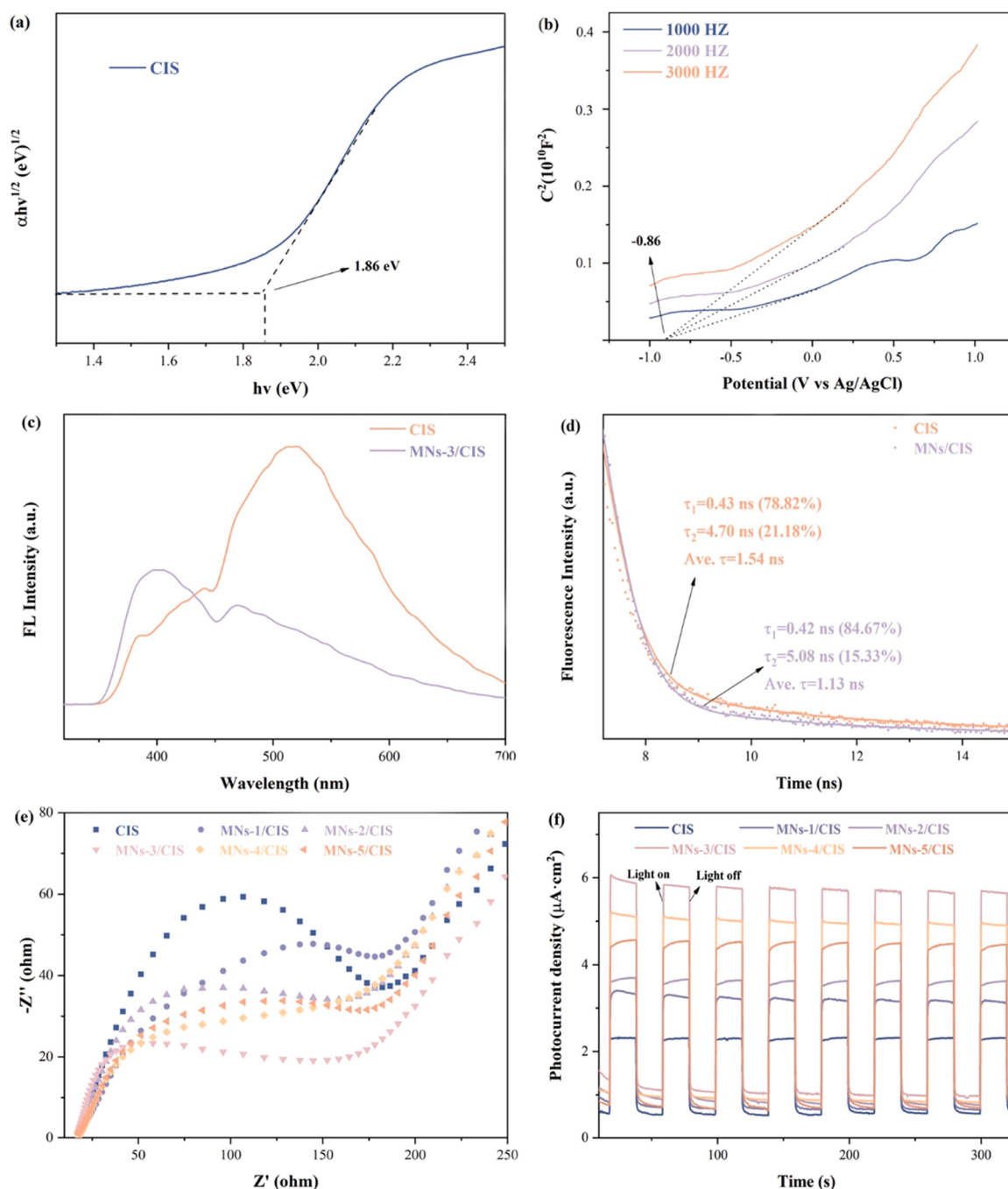


Fig. 6. Plots of $(\alpha h\nu)^{1/2}$ vs. photon energy of CIS (a), the Mott-Schottky plot analysis of CIS (b), Photoluminescence spectra of the CIS and MNs-3/CIS (c), Time-resolved PL decay curves of the CIS and MNs-3/CIS (d), EIS spectra of the photocatalysts under visible-light illumination (e), and nanorods Transient photocurrent response of samples (f).

produce sub-gap exciton states, which can produce redshift PL [41]. Moreover, under the $\lambda = 369.6$ nm pulsed laser excitation, the normalized time-resolved PL decay plots indicated MNs have a high charge separation rate, as presented in Fig. 6d. The average PL decay times (τ_{average}) were found to be 1.13 and 1.54 ns for the MNs/CIS composite and the CIS, respectively. By contrast, the decayed distinctly of MNs/CIS was significantly faster than pristine CIS. In addition, the considerable interaction between the MNs and CIS reflected in the contributions of the fast decay times increased from 78.8% to 84.7%, i.e., τ_1 and τ_2 which are related to charge transfer. As described above, the PL intensity dropped nearly one-half, and faster PL decay means that rapid charge transfer existed between the MNs and CIS, effectively inhibiting the

recombination of severe surface charge under the individual CIS photocatalysts [29,42]. Moreover, EIS measurement was further adopted to investigate the solid interface stratification resistance and the surface charge-transfer resistance that is reflected in arc radius. An arc with a smaller radius for MNs/CIS illustrates the separation of the $e^- - h^+$ pairs more effectively on that species (Fig. 6e). The excellent electrical conductivity and carrier mobility of MNs may result in the weakened electrical resistance of MNs-3/CIS. Moreover, compared with the pristine CIS, the transient photocurrent spectra indicate MNs-3/CIS have a higher photocurrent density. It is further proved that the introduction of MNs improves the light absorption and photocarrier migration and separation efficiency of MNs/CIS (Fig. 6f).

3.4. Possible mechanisms of photocatalytic selective oxidation

To confirm the species and number of photoexcited charge carriers, the molecular oxygen active species was detected [43]. In general, the positive charge carriers were evaluated by h^+ and the O_2 was employed to investigate negative charge carriers [44,45]. The possible active free radicals in the reaction system were identified by EPR. The molecular oxygen active substances were determined by EPR combined with 5, 5-dimethyl-1-pyrroline-N-oxide (DMPO-), whereas 2,2,6,6-tetramethyl piperidinyloxy (TEMPO-) assisted EPR can be used to detect h^+ . Unlike DMPO, TEMPO itself is a paramagnetic material and has an EPR signal. Under the catalyst surface, the h^+ will be generated in the

reaction, which will combine with the single electron of TEMPO, causing a reduction of the signal for TEMPO, and indicating that h^+ is generated during the reaction system. There were no signals for O_2 radicals under dark conditions, demonstrating that no reaction occurred without light, as displayed in Fig. 7a-b. Under simulated sunlight, the signals of O_2 appeared, and the intensity of the characteristic peaks of TEMPO decreased. Due to the number of free radicals would be in proportional to O_2 signal intensity square [46], we compared the signal peak intensities of O_2 and h^+ between different materials and found that MNs-3/CIS produced significantly more O_2 and h^+ (Fig. 7c-d). Therefore, EPR further proves that MNs/CIS greatly accelerated the photo-generated carriers' separation and migration rate.

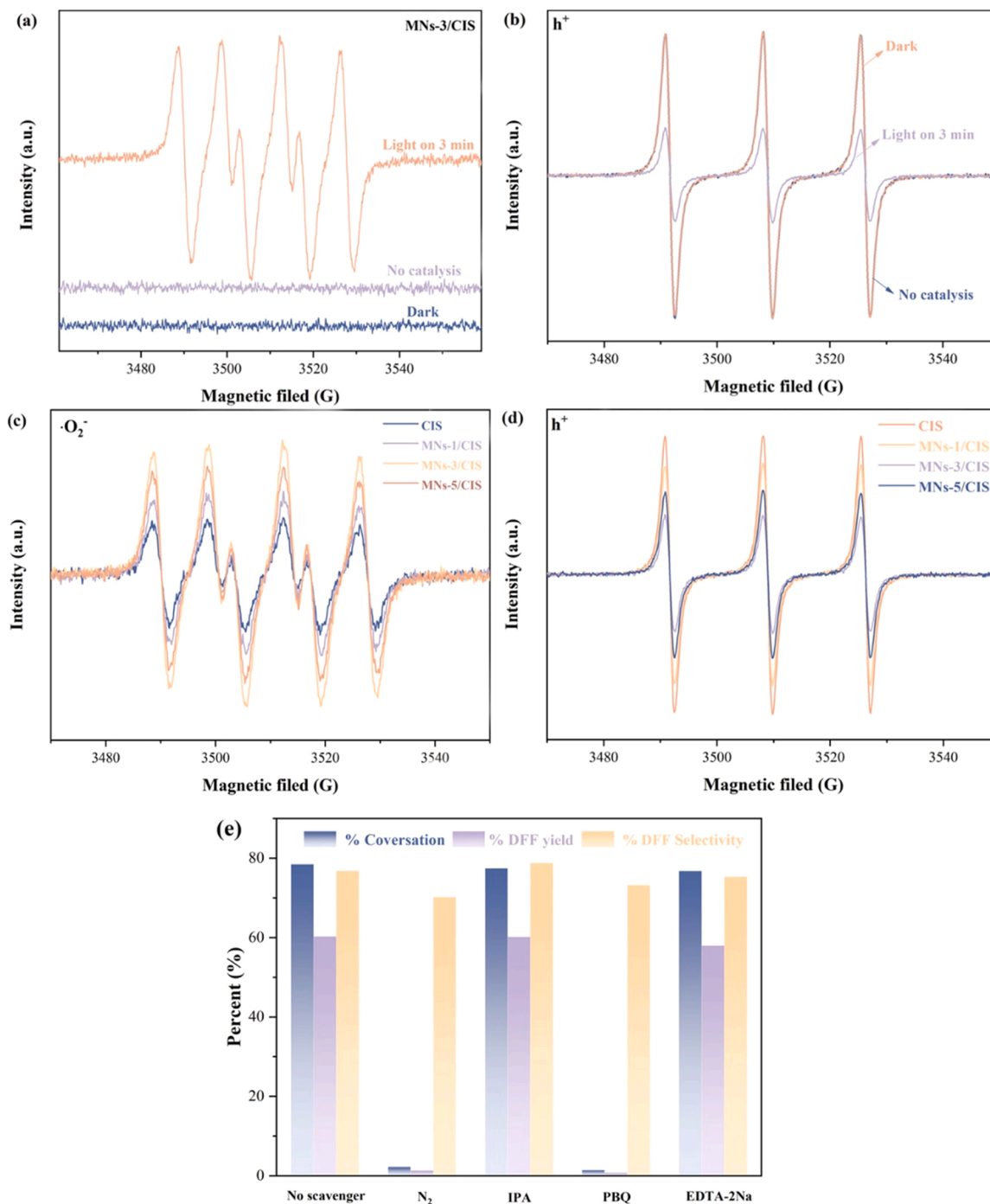


Fig. 7. EPR spectra of MNs-3/CIS under different conditions: O_2 (a), h^+ (b), ESR spectra of CIS, MNs-1/CIS, MNs-3/CIS, and MNs-5/CIS in the presence of O_2 (c) and h^+ (d), The effects of different scavengers on the photocatalytic oxidation reaction behavior (e).

Through a series of trapping agent experiments, the main activated free radicals of the reaction were determined. Hydroquinone (PBQ), isopropanol (IPA), and ethylenediaminetetraacetic acid disodium (EDTA-2Na) were selected as the scavengers of $\text{O}_2^{\cdot-}$, OH^{\cdot} , and h^+ , respectively. Each capture agent concentration was set at 10^{-4} mol/L under the reaction system. When IPA was added, there was no remarkable change in the percent of MNs-3/CIS to HMF conversion. Thus, it can be identified that the existence of hydroxyl radicals is not the decisive factor for the partial oxidation of HMF. Moreover, the catalytic conversion efficiency of HMF was not affected by the addition of EDTA-2Na. It has been reported that the addition of an h^+ trapping agent under general conditions can inhibit the recombination rate of the photogenerated e^- - h^+ pair, thus improving the photocatalytic performance of the material [19,47,48]. But in MNs/CIS photocatalytic system, because of the existence of Schottky junction photoproduction electron effective enrichment MNs above and will not return to CIS, to make the light raw photogenerated e^- - h^+ pairs for effective separation, adding h^+ trapping agent does not improve the separation efficiency of photogenerated e^- - h^+ pairs and further proved the superiority of MNs/CIS Schottky junction. When PBQ was added, the reaction almost stopped. Hence, it can be determined that $\text{O}_2^{\cdot-}$ is the main active substance for the partial oxidation of HMF to DFF in the aqueous phase, which is the same as the photooxidation of aromatic alcohols in organic agents [49]. To determine the source of $\text{O}_2^{\cdot-}$ in the system, we changed the atmosphere from air to N_2 under the same reaction conditions and found that the reaction virtually stopped, proving that the oxidant during the photocatalytic oxidation of HMF to DFF is oxygen molecules from the air (Fig. 7e).

According to the aforementioned results, we propose the mechanism of the catalytic oxidation of HMF to DFF under mild conditions using MNs/CIS heterostructure photocatalytic materials. During the visible-light irradiation, the cubic CIS shows the generation of photogenerated e^- and h^+ . Because the work function of MNs is lower than CIS, the CIS conduction band bends upward, forming a Schottky junction. And due to the conductivity of MNs, the photogenerated electrons of the CIS conduction band migrate to the MNs. The photogenerated electrons retained on the MNs combine with atmospheric oxygen to generate $\text{O}_2^{\cdot-}$ and further oxidized HMF to form DFF. The possible pathways of the photocatalytic oxidation of HMF to DFF by an MNs/CIS heterostructure as shown in Fig. 8.

4. Conclusion

In summary, a promising Schottky junction photocatalytic material was developed by integrating MNs and CIS. The constructed multidimensional MNs/CIS heterostructure has a close limiting surface contact, visible light response, accelerated e^- - h^+ separation, and more efficient charge transport, all of these could be facilitation for the HMF Selective oxidation to DFF. In addition, the Schottky junction formed by n-type semiconductor (CIS) and metal-like semiconductor (MNs) inhibits electron backflow under the heterojunction which further promotes the photoexcited e^- - h^+ pairs separation. Here we fully confirm the photocatalytic mechanism of the MNs/CIS Schottky junction through experiments and theoretical analysis, providing enlightenment for the construction and development of applications of MNs-based heterojunctions. It is envisaged that this synthesis tactic can be expanded to produce a series of new-type MNs-based Schottky junctions, which can be used for biomass value-added conversion.

CRediT authorship contribution statement

Ming Zhang: Conceptualization, Data curation, Writing – original draft. **Yuxin Zhang:** Methodology, Project administration. **Lei Ye:** Data curation, Supervision. **Zhihao Yu:** Formal analysis, Project administration. **Runyu Liu:** Writing – review & editing. **Yina Qiao:** Formal analysis, Supervision. **Linhao Sun:** Visualization. **Jifang Cui:** Project

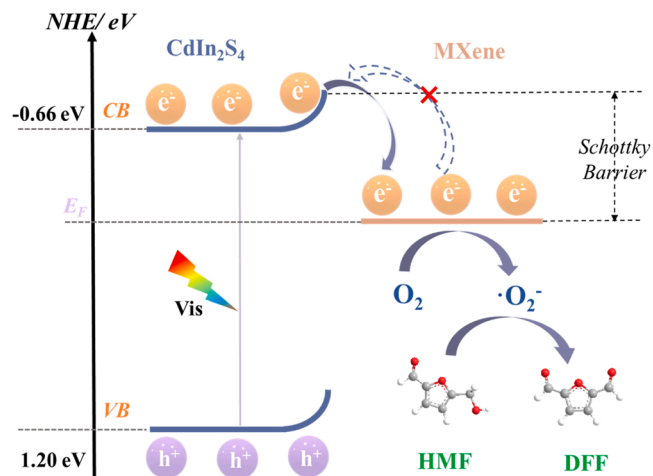


Fig. 8. Possible mechanism for photocatalytic oxidation of HMF to DFF upon MNs/CIS.

administration, Investigation. **Xuebin Lu:** Conceptualization, Funding acquisition, Resources, Supervision, Writing – review & editing.

Declaration of Competing Interest

The authors declare that they have no known competing financial interests or personal relationships that could have appeared to influence the work reported in this paper.

Data Availability

The data that has been used is confidential.

Acknowledgments

This work was supported by the National Natural Science Foundation of China (Grant No. 52066017, 51876180, 51908400).

Appendix A. Supporting information

Supplementary data associated with this article can be found in the online version at [doi:10.1016/j.apcatb.2023.122635](https://doi.org/10.1016/j.apcatb.2023.122635).

References

- [1] U. Nwosu, A. Wang, B. Palma, H. Zhao, M.A. Khan, M. Kibria, J. Hu, Selective biomass photoreforming for valuable chemicals and fuels: a critical review, *Renew. Sustain. Energy Rev.* 148 (2021), 111266, <https://doi.org/10.1016/j.rser.2021.111266>.
- [2] K.A. Davis, S. Yoo, E.W. Shuler, B.D. Sherman, S. Lee, G. Leem, Photocatalytic hydrogen evolution from biomass conversion, *Nano Converg.* 8 (2021), <https://doi.org/10.1186/s40580-021-00256-9>.
- [3] N. Ibrahim, S.K. Kamarudin, L.J. Minggu, Biofuel from biomass via photo-electrochemical reactions: an overview, *J. Power Sources* 259 (2014) 33–42, <https://doi.org/10.1016/j.jpowsour.2014.02.017>.
- [4] A.M. Ruppert, K. Weinberg, R. Palkovits, Hydrogenolysis goes bio: from carbohydrates and sugar alcohols to platform chemicals, *Angew. Chem. Int. Ed.* 51 (2012) 2564–2601, <https://doi.org/10.1002/anie.201105125>.
- [5] Z. Yu, X. Lu, X. Wang, J. Xiong, X. Li, R. Zhang, N. Ji, Metal-Catalyzed hydrogenation of biomass-derived furfural: particle size effects and regulation strategies, *ChemSusChem* 13 (2020) 5185–5198, <https://doi.org/10.1002/cssc.202001467>.
- [6] J.C. Colmenares, Selective redox photocatalysis: is there any chance for solar bio-refineries Juan Carlos Colmenares, *Curr. Opin. Green Sustain. Chem.* 15 (2019) 38–46, <https://doi.org/10.1016/j.cogsc.2018.08.008>.
- [7] L. Hu, A. He, X. Liu, J. Xia, J. Xu, S. Zhou, J. Xu, Biocatalytic transformation of 5-Hydroxymethylfurfural into high-value derivatives: recent advances and future aspects, *ACS Sustain. Chem. Eng.* 6 (2018) 15915–15935, <https://doi.org/10.1021/acssuschemeng.8b04356>.
- [8] H. Wang, C. Zhu, D. Li, Q. Liu, J. Tan, C. Wang, C. Cai, L. Ma, Recent advances in catalytic conversion of biomass to 5-hydroxymethylfurfural and 2, 5-

- dimethylfuran, *Renew. Sustain. Energy Rev.* 103 (2019) 227–247, <https://doi.org/10.1016/j.rser.2018.12.010>.
- [9] L. Hu, J. Xu, S. Zhou, A. He, X. Tang, L. Lin, J. Xu, Y. Zhao, Catalytic advances in the production and application of biomass-derived 2,5-Dihydroxymethylfurfural, *ACS Catal.* 8 (2018) 2959–2980, <https://doi.org/10.1021/acscatal.7b03530>.
 - [10] C. Li, Y. Na, Recent Advances in Photocatalytic Oxidation of 5-Hydroxymethylfurfural, *ChemPhotoChem* 5 (2021) 502–511, <https://doi.org/10.1002/cptc.202000261>.
 - [11] X. Wu, S. Xie, H. Zhang, Q. Zhang, B.F. Sels, Y. Wang, Metal Sulfide Photocatalysts for Lignocellulose Valorization, *ADV Mater.* 33 (2021) 2007129, <https://doi.org/10.1002/adma.202007129>.
 - [12] X. Wu, N. Luo, S. Xie, H. Zhang, Q. Zhang, F. Wang, Y. Wang, Photocatalytic transformations of lignocellulosic biomass into chemicals, *Chem. Soc. Rev.* 49 (2020) 6198–6223, <https://doi.org/10.1039/D0CS00314J>.
 - [13] L. Marzo, S.K. Pagire, O. Reiser, B. König, Photokatalyse mit sichtbarem Licht: Welche Bedeutung hat sie für die organische Synthese? *Angew. Chem. Int. Ed.* 130 (2018) 10188–10228, <https://doi.org/10.1002/ange.201709766>.
 - [14] A. Khan, M. Goepel, A. Kubas, D. Łomot, W. Lisowski, D. Lisovyt'skiy, A. Nowicka, J.C. Colmenares, R. Glaser, Selective oxidation of 5-Hydroxymethylfurfural to 2,5-Diformylfuran by visible light-driven photocatalysis over in situ substrate-sensitized titania, *ChemSusChem* 14 (2021) 1351–1362, <https://doi.org/10.1002/cssc.202002687>.
 - [15] J. Nie, J. Xie, H. Liu, Efficient aerobic oxidation of 5-hydroxymethylfurfural to 2,5-diformylfuran on supported Ru catalysts, *J. Catal.* 301 (2013) 83–91, <https://doi.org/10.1016/j.jcat.2013.01.007>.
 - [16] D.A. Giannakoudakis, A. Qayyum, M. Barczak, R.F. Colmenares-Quintero, P. Borowski, K. Triantafyllidis, J.C. Colmenares, Mechanistic and kinetic studies of benzyl alcohol photocatalytic oxidation by nanostructured titanium (hydro)oxides: do we know the entire story? *Appl. Catal. B* 320 (2023), 121939 <https://doi.org/10.1016/j.apcatb.2022.121939>.
 - [17] Q. Zhang, H. Zhang, B. Gu, Q. Tang, Q. Cao, W. Fang, Sunlight-driven photocatalytic oxidation of 5-hydroxymethylfurfural over a cuprous oxide-anatase heterostructure in aqueous phase, *Appl. Catal. B* 320 (2023), 122006, <https://doi.org/10.1016/j.apcatb.2022.122006>.
 - [18] G. Han, Y. Jin, R.A. Burgess, N.E. Dickenson, X. Cao, Y. Sun, Visible-Light-Driven valorization of biomass intermediates integrated with H₂ production catalyzed by ultrathin Ni/CdS nanosheets, *J. Am. Chem. Soc.* 139 (2017) 15584–15587, <https://doi.org/10.1021/jacs.7b08657>.
 - [19] M. Zhang, Z. Yu, J. Xiong, R. Zhang, X. Liu, X. Lu, One-step hydrothermal synthesis of Cd₃In₂S₈(x+1.5y) for photocatalytic oxidation of biomass-derived 5-hydroxymethylfurfural to 2, 5-diformylfuran under ambient conditions, *Appl. Catal. B* 300 (2022), 120738, <https://doi.org/10.1016/j.apcatb.2021.120738>.
 - [20] X. Bao, M. Liu, Z. Wang, D. Dai, P. Wang, H. Cheng, Y. Liu, Z. Zheng, Y. Dai, B. Huang, Photocatalytic selective oxidation of HMF coupled with H₂ evolution on flexible ultrathin g-C₃N₄ nanosheets with enhanced N–H interaction, *ACS Catal.* 12 (2022) 1919–1929, <https://doi.org/10.1021/acscatal.1c05357>.
 - [21] Y. Tan, Z. Chai, B. Wang, S. Tian, X. Deng, Z. Bai, L. Chen, S. Shen, J. Guo, M. Cai, C. Au, S. Yin, Boosted photocatalytic oxidation of toluene into benzaldehyde on CdIn₂S₄-CdS: synergistic effect of compact heterojunction and S-Vacancy, *ACS Catal.* 11 (2021) 2492–2503, <https://doi.org/10.1021/acscatal.0c05703>.
 - [22] M. Liu, Y. Chen, J. Su, J. Shi, X. Wang, L. Guo, Photocatalytic hydrogen production using twinned nanocrystals and an unanchored NiSx co-catalyst, *Nat. Energy* 1 (2016) 16151, <https://doi.org/10.1038/nenergy.2016.151>.
 - [23] P. Kar, S. Farsinezhad, N. Mahdi, Y. Zhang, U. Obuekwe, H. Sharma, J. Shen, N. Semagina, K. Shankar, Enhanced CH₄ yield by photocatalytic CO₂ reduction using TiO₂ nanotube arrays grafted with Au, Ru, and ZnPd nanoparticles, *Nano Res.* 9 (2016) 3478–3493, <https://doi.org/10.1007/s12274-016-1225-4>.
 - [24] Q. Lang, Y. Yang, Y. Zhu, W. Hu, W. Jiang, S. Zhong, P. Gong, B. Teng, L. Zhao, S. Bai, High-index facet engineering of PtCu cocatalysts for superior photocatalytic reduction of CO₂ to CH₄, *J. Mater. Chem. A* 5 (2017) 6686–6694, <https://doi.org/10.1039/C7TA00737J>.
 - [25] Z. Zeng, Y. Yan, J. Chen, P. Zan, Q. Tian, P. Chen, Boosting the photocatalytic ability of Cu₂O nanowires for CO₂ conversion by MXene quantum dots, *Adv. Funct. Mater.* 29 (2019) 1806500, <https://doi.org/10.1002/adfm.201806500>.
 - [26] R. Xiao, C. Zhao, Z. Zou, Z. Chen, L. Tian, H. Xu, H. Tang, Q. Liu, Z. Lin, X. Yang, In situ fabrication of 1D CdS nanorod/2D Ti₃C₂ MXene nanosheet Schottky heterojunction toward enhanced photocatalytic hydrogen evolution, *Appl. Catal. B* 268 (2020), 118382, <https://doi.org/10.1016/j.apcatb.2019.118382>.
 - [27] J. Li, Y. Li, F. Zhang, Z. Tang, Y. Xu, Visible-light-driven integrated organic synthesis and hydrogen evolution over 1D/2D CdS-Ti₃C₂ MXene composites, *Appl. Catal. B* 269 (2020), 118783, <https://doi.org/10.1016/j.apcatb.2020.118783>.
 - [28] C. Yang, Q. Tan, Q. Li, J. Zhou, J. Fan, B. Li, J. Sun, K. Lv, 2D/2D Ti₃C₂ MXene/g-C₃N₄ nanosheets heterojunction for high efficient CO₂ reduction photocatalyst: dual effects of urea, *Appl. Catal. B* 268 (2020), 118738, <https://doi.org/10.1016/j.apcatb.2020.118738>.
 - [29] Y. Xu, M. Yang, B. Chen, X. Wang, H. Chen, D. Kuang, C. Su, A. CsPbBr₃, Perovskite quantum dot/graphene oxide composite for photocatalytic CO₂ reduction, *J. Am. Chem. Soc.* 139 (2017) 5660–5663, <https://doi.org/10.1021/jacs.7b00489>.
 - [30] G. Zuo, Y. Wang, W.L. Teo, A. Xie, Y. Guo, Y. Dai, W. Zhou, D. Jana, Q. Xian, W. Dong, Y. Zhao, Ultrathin ZnIn₂S₄ nanosheets anchored on Ti₃C₂T_x MXene for Photocatalytic H₂, *Evol. Angew. Chem. Int. Ed.* 59 (2020) 11287–11292, <https://doi.org/10.1002/anie.202002136>.
 - [31] Y. Zhang, N. Zhang, Z. Tang, Y. Xu, Graphene Transforms Wide Band Gap ZnS to a Visible Light Photocatalyst. The new role of graphene as a macromolecular photosensitizer, *ACS Nano* 6 (2012) 9777–9789, <https://doi.org/10.1021/nm304154s>.
 - [32] X. Cao, Z. Chen, R. Lin, W. Cheong, S. Liu, J. Zhang, Q. Peng, C. Chen, T. Han, X. Tong, Y. Wang, R. Shen, W. Zhu, D. Wang, Y. Li, A photochromic composite with enhanced carrier separation for the photocatalytic activation of benzylic C–H bonds in toluene, *Nat. Catal.* 1 (2018) 704–710, <https://doi.org/10.1038/s41929-018-0128-z>.
 - [33] P. Chen, F. Liu, H. Ding, S. Chen, L. Chen, Y. Li, C. Au, S. Yin, Porous double-shell CdS@C₃N₄ octahedron derived by in situ supramolecular self-assembly for enhanced photocatalytic activity, *Appl. Catal. B* 252 (2019) 33–40, <https://doi.org/10.1016/j.apcatb.2019.04.006>.
 - [34] X. Ye, Y. Chen, C. Ling, J. Zhang, S. Meng, X. Fu, X. Wang, S. Chen, Chalcogenide photocatalysts for selective oxidation of aromatic alcohols to aldehydes using O₂ and visible light: a case study of CdIn₂S₄, CdS and In₂S₃, *CHEM ENG J.* 348 (2018) 966–977, <https://doi.org/10.1016/j.cej.2018.05.035>.
 - [35] Z. Zhang, J.T. Yates, Band bending in semiconductors: chemical and physical consequences at surfaces and interfaces, *Chem. Rev.* 112 (2012) 5520–5551, <https://doi.org/10.1021/cr3000626>.
 - [36] F. Liu, C. Xiao, L. Meng, L. Chen, Q. Zhang, J. Liu, S. Shen, J. Guo, C. Au, S. Yin, Facile fabrication of octahedral CdS–ZnS by cation exchange for photocatalytic toluene selective oxidation, *ACS Sustain. Chem. Eng.* 8 (2020) 1302–1310, <https://doi.org/10.1021/acssuschemeng.9b06802>.
 - [37] S. Wang, B.Y. Guan, Y. Lu, X.W.D. Lou, Formation of Hierarchical In₂S₃-CdIn₂S₄ heterostructured nanotubes for efficient and stable visible light CO₂ reduction, *J. Am. Chem. Soc.* 139 (2017) 17305–17308, <https://doi.org/10.1021/jacs.7b10733>.
 - [38] S. Cao, B. Shen, T. Tong, J. Fu, J. Yu, 2D/2D heterojunction of ultrathin MXene/Bi₂WO₆ nanosheets for improved photocatalytic CO₂ reduction, *Adv. Funct. Mater.* 28 (2018) 1800136, <https://doi.org/10.1002/adfm.201800136>.
 - [39] A. Pan, X. Ma, S. Huang, Y. Wu, M. Jia, Y. Shi, Y. Liu, P. Wangyang, L. He, Y. Liu, CsPbBr₃ perovskite nanocrystal grown on MXene nanosheets for enhanced photoelectric detection and photocatalytic CO₂ reduction, *J. Phys. Chem. Lett.* 10 (2019) 6590–6597, <https://doi.org/10.1021/acs.jpclett.9b02605>.
 - [40] B. Bharti, S. Kumar, H. Lee, R. Kumar, Formation of oxygen vacancies and Ti3+ state in TiO₂ thin film and enhanced optical properties by air plasma treatment, *Sci. Rep-UK* 6 (2016), <https://doi.org/10.1038/srep32355>.
 - [41] Y. Shao, W. Gao, H. Yan, R. Li, I. Abdelwahab, X. Chi, L. Rogée, L. Zhuang, W. Fu, S.P. Lau, S.F. Yu, Y. Cai, K.P. Loh, K. Leng, Unlocking surface octahedral tilt in two-dimensional Ruddlesden-Popper perovskites, *Nat. Commun.* 13 (2022), <https://doi.org/10.1038/s41467-021-27747-x>.
 - [42] M.D. Regulacio, M. Han, Multinary I-III-VI₂ and II-II-IV-VI₄ semiconductor nanostructures for photocatalytic applications, *Acc. Chem. Res.* 49 (2016) 511–519, <https://doi.org/10.1021/acs.accounts.5b00535>.
 - [43] L. Wang, X. Zhao, D. Lv, C. Liu, W. Lai, C. Sun, Z. Su, X. Xu, W. Hao, S.X. Dou, Y. Du, Promoted photocharge separation in 2D lateral epitaxial heterostructure for visible-light-driven CO₂ photoreduction, *Adv. Mater.* 32 (2020) 2004311, <https://doi.org/10.1002/adma.202004311>.
 - [44] H. Huang, X. Li, J. Wang, F. Dong, P.K. Chu, T. Zhang, Y. Zhang, Self-Doping as a Promising Strategy: band-gap engineering and multi-functional applications of high-performance CO₃²⁻-Doped Bi₂O₂CO₃ (Anionic Group), *ACS Catal.* 5 (2015) 4094–4103, <https://doi.org/10.1021/acscatal.5b00444>.
 - [45] H. Huang, S. Tu, C. Zeng, T. Zhang, A.H. Reshak, Y. Zhang, Macroscopic polarization enhancement promoting photo- and piezoelectric-induced charge separation and molecular oxygen activation, *Angew. Chem. Int. Ed.* 56 (2017) 11860–11864, <https://doi.org/10.1002/anie.201706549>.
 - [46] Y. Li, S. Ouyang, H. Xu, X. Wang, Y. Bi, Y. Zhang, J. Ye, Constructing solid–gas–interfacial fenton reaction over Alkalized-C₃N₄ photocatalyst to achieve apparent quantum yield of 49% at 420 nm, *J. Am. Chem. Soc.* 138 (2016) 13289–13297, <https://doi.org/10.1021/jacs.6b07272>.
 - [47] H. Zhang, Q. Wu, C. Guo, Y. Wu, T. Wu, Photocatalytic selective oxidation of 5-Hydroxymethylfurfural to 2,5-Diformylfuran over Nb₂O₅ under visible light, *ACS Sustain. Chem. Eng.* 5 (2017) 3517–3523, <https://doi.org/10.1021/acssuschemeng.7b00231>.
 - [48] I. Krivtsov, E.I. García-López, G. Marci, L. Palmisano, Z. Amghouz, J.R. García, S. Ordóñez, E. Díaz, Selective photocatalytic oxidation of 5-hydroxymethyl-2-furfural to 2,5-furandicarboxaldehyde in aqueous suspension of g-C₃N₄, *Appl. Catal. B: Environ.* 204 (2017) 430–439, <https://doi.org/10.1016/j.apcatb.2016.11.049>.
 - [49] F. Su, S.C. Mathew, G. Lipner, X. Fu, M. Antonietti, S. Blechert, X. Wang, mpg-C₃N₄-Catalyzed selective oxidation of alcohols using O₂ and Visible Light, *J. Am. Chem. Soc.* 132 (2010) 16299–16301, <https://doi.org/10.1021/ja102866p>.